Research Square

Preprints are preliminary reports that have not undergone peer review.
They should not be considered conclusive, used to inform clinical practice,
or referenced by the media as validated information.

Construction and modularization of Li(NiCoMn)/CNOCl nanocages by using cathode materials of retired lithium batteries and their unique advanced oxidation performance

Yawen Li
Hebei University of Science and Technology
Kai Deng
Hebei University of Science and Technology
Lingxiao Jiang
Jiang Xi Ecological Environmental Monitoring Center
Kexin Li
likexin_chem@163.com

Hebei University of Science and Technology https://orcid.org/0000-0001-6774-9479

Research Article

Keywords: Carbon oxynitride, Li(NiCoMn)O2, Nanocage, Modular photocatalyst, Synergistic advanced oxidation

Posted Date: August 24th, 2026

DOI: https://doi.org/10.21203/rs.3.rs-10354015/v1

License: This work is licensed under a Creative Commons Attribution 4.0 International License.
Read Full License

Abstract

In this paper, a series of metal ion cluster-loaded chlorine-doped carbon oxynitride nanocage powder photocatalysts (Li(NiCoMn)-*x*/CNOCl) and modular photocatalysts supported by polymeric sodium alginate gel spheres (Li(NiCoMn)-10/CNOCl@PSA) were successfully constructed by using $Li(NiCoMn)O_2$ derived from retired lithium battery cathode materials as a precursor via a simple process. Li(NiCoMn) metal ion clusters play key roles in Li(NiCoMn)-*x*/CNOCl powder photocatalysts: constructing the nanocage micromorphology, improving the separation efficiency of photogenerated carriers ($e^- – h^+$), and activating potassium peroxymonosulfate ($KHSO_5$). The modular photocatalyst Li(NiCoMn)-10/CNOCl@PSA increases the potential engineering application value of Li(NiCoMn)-*x*/CNOCl powder photocatalysts, while the Li(NiCoMn) metal ion cluster crosslinking centers in PSA carrier can activate $KHSO_5$. The performance of the powder and modular photocatalysts in degrading typical organic pollutants in water and depolymerizing natural lignin to produce vanillin through photocatalytic oxidation, activated $KHSO_5$ oxidation, and synergistic advanced oxidation processes. Finally, a generally applicable advanced oxidation thermodynamic model was constructed.

1. Introduction

Ternary polymer lithium battery (TPLB) has been widely used as the power battery of electric vehicles at present, based on the advantages of high energy density, good safety performance, and strong adaptability [1–6]. However, when the TPLB reaches its full cycle life, the harmless treatment and high value-added reuse of waste TPLB are serious challenges in the process of human sustainable development. TPLB are mainly composed of cathode material ($Li(NiCoMn)O_2$ or $Li(NiCoAl)O_2$), anode material (graphite), and electrolyte (organic solvents, inorganic salts, and additives) [7, 8]. Among them, the mass fraction of cathode material is about 60 ~ 70%, which accounts for the equipment quality of the whole TPLB [9]. In recent years, some researchers have done a lot of valuable research on the recovery of cathode materials for retired lithium batteries and the improvement of specific electrodes and electrocatalysis based on low-cost metals [10–12]. In the study, we found that $Li(NiCoMn)O_2$ precursor has the following four application values: (1) as a structural director for constructing carbon oxynitride (CNO) with nanocage micromorphology; (2) improving the separation efficiency of photogenerated carriers ($e^- – h^+$) of CNO; (3) activating $KHSO_5$; (4) as a cross-linking agent for preparing polymeric sodium alginate (PSA) carrier.

Graphitic carbon nitride (g-C_3N_4) and its modified composites have attracted much attention in the field of environmental photocatalysis, which has the advantages of environmental friendliness, visible-light response, and low cost [13–17]. However, the visible-light photocatalytic activity of g-C_3N_4 is poor because of the high mass transfer resistance caused by multi-layer structure and the low separation efficiency of photogenerated $e^- – h^+$ [18]. In addition, the physical state of powder also limits the practical application of g-C_3N_4 [19]. Both melamine ($C_3H_6N_6$) and urea (CH_4N_2O) can be used as precursors to synthesize g-C_3N_4, and the g-C_3N_4 synthesized from urea has higher visible-light photocatalytic activity

compared with the g-C_3N_4 synthesized from melamine [20, 21]. Because the g-C_3N_4 synthesized from urea contains oxygen, we define the g-C_3N_4 prepared from urea as carbon oxynitride and abbreviated it as CNO. In the study, we found that as a precursor in the synthesis process, Li(NiCoMn)O_2 can not only construct CNO with nanocage micromorphology, but also significantly improve the photogenerated e^-–h^+ separation efficiency of CNO, thus improving the visible-light photocatalytic activity of CNO in an all-round way. Some researchers have developed some photocatalysts using Li(NiCoMn)O_2 as the precursor. However, these photocatalysts generally have some problems, such as complex synthesis process, poor visible-light activity and neglect of morphology control [22–24].

The concept of "nano-confined catalysis" was first put forward by the team of academician Xinhe Bao from Dalian Institute of Chemical Physics, Chinese Academy of Sciences [25–27]. In short, "nano-confined catalysis" is to provide a constrained environment for the catalytic reaction on the nano scale, so as to realize the precise regulation of catalytic performance [28–30]. The C_3N_4 nanotubes prepared in our previous work [31–33] and the CNO nanocages prepared in this paper belong to "nano-confined photocatalyst". The above-mentioned special nanostructures enhance the passage of the reaction solvent, thus reducing the mass transfer resistance of the photocatalytic reaction, while the target degradation object is trapped in the nano-scale space, thus being degraded by photocatalysis more effectively.

Compared with single photocatalytic oxidation technology, synergistic advanced oxidation technology can accelerate the degradation of organic pollutants (OPs) in water, and can also degrade OPs in water that can not be degraded by photocatalytic oxidation or single oxidation process [34–37]. Our research shows that a certain amount of potassium peroxymonosulfate ($KHSO_5$) is added to the photocatalytic reaction system to form a synergistic advanced oxidation system. On the one hand, photogenerated electrons and Li(NiCoMn) metal ion clusters can activate $KHSO_5$ through electron transfer mechanism, thus achieving a synergistic advanced oxidation effect. On the other hand, photogenerated electrons can also reduce high-valence transition metal ions to low-valence states, so that the synergistic advanced oxidation reaction can continue. Some researchers have reported the study of removing OPs from water by activating $KHSO_5$ with photogenerated electrons or low-valence transition metal ions [38, 39]. However, there are few reports about the simultaneous activation of $KHSO_5$ by photogenerated electrons and low-valence transition metal ions and the discussion of the law of electron transfer in the whole synergistic advanced oxidation system.

The difficulty of separation and reuse is the bottleneck problem that restricts the practical application of powder photocatalyst [40–43]. Therefore, the construction of modular photocatalysts is the effective way for photocatalytic technology from theoretical research to practical application. In the study, we found that PSA can be used as a carrier of powder photocatalyst, and Li(NiCoMn) metal ion clusters can be used as the crosslinking agent for preparing PSA. Modular photocatalyst prepared with PSA as carrier is not only similar to powder photocatalyst in photocatalytic activity, but also PSA carrier itself can activate $KHSO_5$ due to the existence of Li(NiCoMn) metal ion cluster cross-linking centers.

In this paper, we successfully prepared a series of Li(NiCoMn)-*x*/CNOCl powder photocatalysts with cathode material Li(NiCoMn)O_2 of retired lithium battery and urea as raw materials by one-step thermal polymerization strategy. In the synthesis process, Li(NiCoMn)O_2 not only constructs the nanocage micromorphology of Li(NiCoMn)-*x*/CNOCl by preventing the condensation of terminal amino ($-NH_2$) and/or hydroxyl (−OH) groups, but also significantly improves the photogenerated e^-–h^+ separation efficiency of Li(NiCoMn)-*x*/CNOCl by loading Li(NiCoMn) metal ion clusters. In the process of synergistic advanced oxidation, $KHSO_5$ can be activated by photogenerated electrons and low-valence transition metal ions in Li(NiCoMn) metal ion clusters at the same time, and high-valence transition metal ions can be reduced to low-valence states by photogenerated electrons, so the degradation efficiency of target OPs in the synergistic advanced oxidation process is very high. In order to solve the problem of difficult separation and reuse of powder photocatalyst, we successfully prepared Li(NiCoMn)-10/CNOCl@PSA modular photocatalyst with PSA as carrier. The as-prepared Li(NiCoMn)-10/CNOCl@PSA modular photocatalyst has similar photocatalytic activity to Li(NiCoMn)-10/CNOCl powder photocatalyst, and the Li(NiCoMn) metal ion cluster crosslinking centers in PSA carrier also have the effect of activating $KHSO_5$. In the performance study, we took rhodamine B (RhB), chlortetracycline hydrochloride (CTC), and leucomalachite green (LMC) as the target OPs, systematically studied the activities of the as-prepared powder and modular photocatalysts in photocatalytic oxidation, activated $KHSO_5$ oxidation, and synergistic advanced oxidation processes. In addition, we further explored the performance of the as-prepared powder and modular photocatalysts in the above three reaction processes through the experiment of depolymerizing natural lignin to produce vanillin. Vanillin is an important chemical raw material, which can be used as food additive, pharmaceutical intermediate, and intermediate for synthesizing high-density aviation fuel [44–46]. In this paper, the construction mechanism of the as-prepared powder and modular photocatalysts and the reaction mechanism of three advanced oxidation processes will be discussed in detail.

2. Experimental

The details of the experimental section are shown in the Supplementary Material.

3. Results and discussion

3.1. Characterizations

3.1.1. Morphology

Powder photocatalyst Li(NiCoMn)-10/CNOCl with the best photocatalytic performance was taken as the representative. The morphology was studied by TEM and TEM-HAADF, the crystal phase structure was studied by HRTEM and SAED, and the element composition was studied by EDX elemental mappings. As shown in Fig. 1a, the as-prepared Li(NiCoMn)-10/CNOCl shows a cage-like nanostructure, which can not only reduce the mass transfer resistance of reaction solvent, but also effectively capture and rapidly

degrade the target objects through the “nano-confined catalysis”. As shown in Figs. S1a, b, e, and f, comparing the TEM images of Li(NiCoMn)-10/CNOCl and CNO, we can find that this nanocage micromorphology is exclusive to Li(NiCoMn)-10/CNOCl, while CNO is a non-porous multi-layer structure. The formation of this nanocage micromorphology can be attributed to the fact that Li(NiCoMn)O_2 can be used as a structural director to construct nanocage micromorphology in CNO after chlorination. As shown in Scheme 1a, urea will be preliminarily polycondensed to form four prepolymers during the high-temperature polycondensation reaction. In the subsequent polycondensation reaction, on the one hand, the Li(NiCoMn) metal ion clusters in Li(NiCoMn)Cl_4 will directly prevent the terminal –NH_2 and/or –OH groups from further condensation and chemically bonding with CNO, thus constructing a porous structure; On the other hand, the Cl^- in Li(NiCoMn)Cl_4 will replace the –NH_2 and –OH groups in the prepolymer, thus indirectly preventing the terminal –NH_2 and/or –OH groups from further condensation to form a porous structure. In addition, Cl^- may directly replace the terminal –NH_2 or –OH groups at the end of the materials and form terminal –Cl groups at the boundary of the materials. In our previous work, we pretreated melamine with hydrochloric acid and/or ethylene glycol to obtain similar porous carbon nitride [47, 48]. From TEM-HAADF images, we can clearly observe the three-dimensional cross-linked nanocage micromorphology and bright spherical Li(NiCoMn) metal ion clusters (Figs. 1b and e). As shown in Fig. 1c, a large number of Li(NiCoMn) metal ion clusters with lattice stripes were observed in HRTEM images, which played an important role in improving the separation efficiency of photogenerated e^-–h^+ and activating $KHSO_5$. As shown in Figs. S1c, d, g, and h, by comparing the HRTEM images of Li(NiCoMn)-10/CNOCl and CNO, it can be seen that Li(NiCoMn) metal ion clusters are distributed in various positions of Li(NiCoMn)-10/CNOCl, but the existence of Li(NiCoMn) metal ion clusters cannot be observed in CNO. Diffraction rings corresponding to (100) and (002) crystal planes can be roughly observed from SAED diagram, which is consistent with the result of XRD (Fig. 1d). It can be seen from the EDX elemental mapping images shown in Figs. 1f–l that Li(NiCoMn)-10/CNOCl contains C, N, O, Cl, Ni, Co, and Mn elements, and the existence of Li element needs to be proved by XPS.

The internal morphology of the modular photocatalyst Li(NiCoMn)-10/CNOCl@PSA was studied by FESEM. As shown in Fig. 1m, the as-prepared modular photocatalyst shows a three-dimensional network microstructure similar to an ant nest, and tiny powder photocatalyst block units are firmly embedded in this three-dimensional network through hydrogen bonding (Scheme 1b). Different from the traditional modular photocatalyst, the powder photocatalyst dispersed inside of PSA can effectively contact with the target objects, so the performance of Li(NiCoMn)-10/CNOCl@PSA modular photocatalyst is similar to that of Li(NiCoMn)-10/CNOCl powder photocatalyst (Fig. 4d vs. Figure 4i). As shown in Figs. 1n and o, the pure PSA carrier is transparent, while the PSA loaded with powder photocatalyst appears pale yellow. Transparent PSA carrier will not affect the absorption of photons by the supported powder photocatalyst. As can be seen from Fig. 1p, the adsorption-saturated modular photocatalyst shows the same red color as RhB, which indicates that RhB enters the interior of PSA carrier through the surface micropores, and the confined environment inside PSA carrier is very beneficial to the RhB degradation.

3.1.2. Compositional and structural information

The composition and chemical state of surface elements of Li(NiCoMn)O_2, CNO, and Li(NiCoMn)-10/CNOCl samples were studied by XPS probe technique. As shown in Fig. 2a and Table S1, Li(NiCoMn)O_2 contains five elements of Li, Ni, Co, Mn, and O, CNO contains three elements of C, N, and O, and Li(NiCoMn)-10/CNOCl contains eight elements of Li, Ni, Co, Mn, C, N, O, and Cl. The Cl element in the Li(NiCoMn)-10/CNOCl comes from the intermediate product Li(NiCoMn)Cl_4, which is generated by ionization of Li(NiCoMn)O_2 precursor in dilute HCl. The Cl^- in Li(NiCoMn)Cl_4 replaces the terminal $–NH_2$ or –OH groups in Li(NiCoMn)-10/CNOCl in the process of high temperature polycondensation, thus forming a C-Cl bond at the end of the material (Scheme 1a). The chemical states of Li, Ni, Co, and Mn four metal elements in the Li(NiCoMn)O_2 and Li(NiCoMn)-10/CNOCl samples were studied by their corresponding high-resolution XPS. As shown in Fig. 2b, there are three chemical states of Li element in the Li(NiCoMn)O_2 corresponding to Li–O–Ni, Li–O–Co, and Li–O–Mn structural components. As shown in Figs. 2c–e, for the Li(NiCoMn)O_2, the XPS peaks centered at 855.2 and 872.8 eV correspond to the spin-orbit splitting peaks of Ni $2p_{3/2}$ and Ni $2p_{1/2}$, the XPS peaks centered at 780.2 and 795.3 eV correspond to the spin-orbit splitting peaks of Co $2p_{3/2}$ and Co $2p_{1/2}$, and the XPS peaks centered at 642.6 and 654.4 eV correspond to the spin-orbit splitting peaks of Mn $2p_{3/2}$ and Mn $2p_{1/2}$. Compared with Li(NiCoMn)O_2, the binding energy of Li, Ni, Co, Mn elements in Li(NiCoMn)-10/CNOCl have changed, indicating that the Li(NiCoMn) metal ion clusters interact with the terminal $–NH_2$ and/or –OH groups of CNO through covalent bonds. The chemical states of C, N, O, and Cl four nonmetal elements in the Li(NiCoMn)O_2, CNO, and Li(NiCoMn)-10/CNOCl samples were studied by their corresponding high-resolution XPS. As shown in Fig. 2f, the peak centered at 284.8 eV is typically assigned to the adventitious reference carbon on the surface of the samples. For the CNO, the peak centered at 288.4 eV can be attributed to sp^2 C atoms bonded to N or O in an aromatic ring (N = C-N(N) or N = C-N(O)). Compared with CNO, the XPS peak of sp^2 C in the Li(NiCoMn)-10/CNOCl shows obvious chemical shift due to the substitution of terminal $–NH_2$ or –OH by –Cl to form N = C-N(Cl) covalent bond. As shown in Fig. 2g, for the CNO, the peak centered at 398.8 eV is assigned to sp^2-hybridized aromatic nitrogen atoms bonded to carbon atoms (C = N–C). The peak centered at 400.8 eV is related to either tertiary nitrogen $(C)_3$–N groups linking structural motifs (C_6N_7) or amino groups carrying hydrogen ($(C)_2$–NH or C–NH_2). A weak peak at 404.6 eV corresponds to nitrogen atoms bonded to three carbon atoms in the aromatic cycles (N–$(C)_3$). Compared with CNO, the XPS peaks of N 1s in the Li(NiCoMn)-10/CNOCl have obvious chemical shift due to the interaction between hydrogen-containing amino groups and Li(NiCoMn) metal ion clusters through covalent bonds to form $(C)_2$–N–Li(NiCoMn), C–NH–Li(NiCoMn), and C–N = Li(NiCoMn) covalent bonds. As shown in Fig. 2h, the O element in the Li(NiCoMn)O_2 shows two chemical states, corresponding to the covalent bonds between O atoms and Li atoms and the covalent bonds between O atoms and Ni, Co or Mn atoms. For the CNO, the broad peak centered at 532.5 eV can be attributed to the C–O–C and/or C–OH structural components. Compared with CNO, the XPS peak of O 1s in the Li(NiCoMn)-10/CNOCl is obviously enhanced because more C–O–C and/or C–OH structural components are exposed by the construction of nanocage micromorphology. In addition, the O 1s XPS peak of the Li(NiCoMn)-10/CNOCl shows obvious chemical shift compared with that of

CNO because of the covalent bond interaction between –OH groups and Li(NiCoMn) metal ion clusters to form C–O–Li(NiCoMn). As shown in Fig. 2i, the XPS peaks of Cl 2p centered at 200.0 and 201.1 eV in the Li(NiCoMn)-10/CNOCl can be attributed to the Cl $2p_{3/2}$ and Cl $2p_{1/2}$ spin-orbit splitting peaks. The XPS result of Cl 2p further confirmed that Cl element was introduced into Li(NiCoMn)-10/CNOCl to form C–Cl covalent bonds.

The textural characteristics of as-prepared powder photocatalysts were studied by nitrogen porosity measurement. As shown in Fig. S2a, the type II isotherm with an adsorption amount close to zero for the CNO corresponds to the non-porous characteristic of CNO with multi-layer structure prepared by urea. For the Li(NiCoMn)-*x*/CNOCl samples, the type IV isotherms with H3 hysteresis loops correspond to their mesoporosity due to the construction of nanocage micromorphology. With increasing the dosage of $Li(NiCoMn)O_2$ from 0 to 10 mg, the nanocage micromorphology tends to perfect, so the BET (Brunauer–Emmett–Teller) specific surface areas of Li(NiCoMn)-*x*/CNOCl gradually increase. However, excessive addition of $Li(NiCoMn)O_2$ will lead to the blockage of cage holes, so the BET specific surface areas of Li(NiCoMn)-*x*/CNOCl will gradually decrease. The BJH (Barrett–Joyner–Halenda) pore-size distribution curves reveal that all the tested materials exhibit a narrow peak at 0–5 nm, which can be attributed to the released NH_3 and H_2O that act as soft-templates during the course of urea polycondensation (Fig. S2b). For the Li(NiCoMn)-*x*/CNOCl samples, the broad BJH pore-size distribution curves at 5–60 nm are derived from their nanocage micromorphologies.

The crystal phase structures of as-prepared powder photocatalysts were studied by XRD. As shown in Fig. 3a, CNO sample exhibits a typical (002) interlayer-stacking peak at 27.1^o which corresponds to an interlayer distance of d = 0.33 nm, while the (100) peak at 12.8^o represents in-plane structural packing motif with a period of 0.675 nm. For the Li(NiCoMn)-*x*/CNOCl samples, the weakened diffraction peak of (002) plane and the disappeared diffraction peak of (100) plane show that the layered structure units are reduced due to the construction of nanocage micromorphology. In addition, the XRD diffraction peaks of $Li(NiCoMn)O_2$ can not be observed in the Li(NiCoMn)-*x*/CNOCl samples, indicating that the $Li(NiCoMn)O_2$ precursor was destroyed and reassembled in the Li(NiCoMn)-*x*/CNOCl during the synthesis process.

The chemical structures of as-prepared powder photocatalysts were studied by FTIR spectra. As shown in Fig. 3b, for the CNO and Li(NiCoMn)-*x*/CNOCl samples, a series of peaks found in the range of 1800–1000 cm^{-1} is attributed to the stretching modes like C–N and C = N in the CN heterocycles. The sharp peak at 806.7 cm^{-1} is the typical bending vibration of *s*-triazine units. The broad absorption peaks located in the range of 3500–2800 cm^{-1} originates from the stretching vibrational modes of primary amine ($–NH_2$), secondary amine (= NH), and hydroxyl (–OH) groups. Compared with CNO sample, the enhanced FTIR absorption peaks for the Li(NiCoMn)-*x*/CNOCl samples can be attributed to the exposure of more surface functional groups due to the construction of nanocage micromorphology. In addition, the FTIR absorption peaks of $Li(NiCoMn)O_2$ also can not be observed in the Li(NiCoMn)-*x*/CNOCl

samples, further indicating that the Li(NiCoMn)O_2 precursor was destroyed and reassembled in the Li(NiCoMn)-*x*/CNOCl during the synthesis process.

3.1.3. Optical and electronic properties

The photogenerated e^-–h^+ separation efficiency of as-prepared powder photocatalysts was studied by PL and TR-PL spectra. As shown in Fig. 3c, the PL emission peak in the range of 400–600 nm for CNO can be attributed to the recombination of separated e^-–h^+ in CNO. Compared with CNO, the PL emission peak intensities of Li(NiCoMn)-*x*/CNOCl are significantly reduced, which is because the trapping effect of 3d unsaturated electron orbitals in Ni, Co, and Mn metal atoms on photogenerated electrons significantly slows down the recombination rate of photogenerated e^-–h^+ (Scheme 1a). As shown in Fig. 3d, the TR-PL emission peak intensities of Li(NiCoMn)-*x*/CNOCl are obviously lower than that of CNO, which shows that the number of photogenerated e^-–h^+ recombination in Li(NiCoMn)-*x*/CNOCl is less in unit time, thus further confirming that Li(NiCoMn)-*x*/CNOCl have higher photogenerated e^-–h^+ separation efficiency.

The equivalent circuit diagram of the fitting EIS results is inserted into Fig. 3e. As shown in Fig. 3e, R_s is the resistance of the solution, R_{ct} is the resistance in electron transfer, and CPE is the constant phase element [49]. Compared with CNO, the EIS semi-cycle radii of Li(NiCoMn)-*x*/CNOCl are decreased, indicating that the transmission resistance of photogenerated e^-–h^+ decreases due to the induced effect of 3d unsaturated electron orbitals in Ni, Co, and Mn metal atoms on photogenerated electrons.

As shown in Fig. 3f, the prompt increase in transient photocurrent from the light-off to the light-on state is ascribed to the quick separation and transfer of photogenerated e^-–h^+ on the surfaces of working electrodes. Compared with CNO, the increased transient photocurrents of Li(NiCoMn)-*x*/CNOCl can be attributed to the induced effect of 3d unsaturated electron orbitals in Ni, Co, and Mn metal atoms on photogenerated electrons, which accelerates the directional transmission of photogenerated e^-–h^+.

The light absorption properties of as-prepared powder photocatalysts were studied by UV–vis/DRS. As shown in Fig. 3g, CNO shows a typical semiconductor absorption within the region of 200–450 nm, which originates from the electron transfer response from valence band (VB) to the conduction band (CB). Compared with CNO, the enhanced light absorption capacity of Li(NiCoMn)-*x*/CNOCl in the range of 200–800 nm can be attributed to the trapping effect of Li(NiCoMn) metal ion clusters on photons in this spectral range. The enhancement of light absorption capacity is beneficial for photocatalyst to capture photons, thus improving the photoelectric conversion efficiency of photocatalyst. In addition, the absorption bands of Li(NiCoMn)-*x*/CNOCl are redshifted relative to that of CNO, because the introduction of Ni, Co, Mn, and Cl elements leads to the distortion of CB and VB, which reduces the band gap energies of Li(NiCoMn)-*x*/CNOCl (Scheme 1a).

The CB potentials (E_{CB}) of as-prepared CNO and Li(NiCoMn)-10/CNOCl were determined by their corresponding Mott-Schottky plots. As shown in Fig. 3h, the flat band potentials (V_{fb}) obtained by extrapolation of the Mott-Schottky plots are − 0.59 and − 0.75 V for CNO and Li(NiCoMn)-10/CNOCl

versus Ag/AgCl. After correction by adding + 0.22 V, the E_{CB} of CNO and Li(NiCoMn)-10/CNOCl are − 0.37 and − 0.53 V, respectively. The VB potentials (E_{VB}) of as-prepared CNO and Li(NiCoMn)-10/CNOCl were determined by the VB-XPS. As shown in Fig. 3i, the E_{VB} of CNO and Li(NiCoMn)-10/CNOCl are 2.34 and 2.04 eV, respectively. The changes of E_{CB} and E_{VB} of CNO after the introduction of Li(NiCoMn) metal ion clusters and –Cl groups can be attributed to the distortion of CB and VB caused by the energy band hybridization (Scheme 1a). According to the Mott-Schottky and VB-XPS results, the band gap energies of CNO and Li(NiCoMn)-10/CNOCl are 2.71 and 2.57 eV, respectively.

3.2. Performance tests

3.2.1. Chemical significance of advanced oxidation macrothermodynamic model

In the performance tests, we found that the as-prepared Li(NiCoMn)-*x*/CNOCl powder photocatalysts and Li(NiCoMn)-10/CNOCl@PSA modular photocatalyst showed unique advanced oxidation performance in photocatalytic oxidation, activated $KHSO_5$ oxidation, and synergistic advanced oxidation processes. Therefore, we constructed an advanced oxidation macrothermodynamic model to reasonably explain the unique advanced oxidation performance of the as-prepared powder and modular photocatalysts in the three different advanced oxidation processes mentioned above. The chemical significance of advanced oxidation macrothermodynamic model is that all elementary reactions in the process of advanced oxidation are ignored, and the reaction rate of advanced oxidation depends on the electron transfer efficiency from reductant to oxidant. All the performance test results of this paper will be reasonably explained according to the constructed advanced oxidation macrothermodynamic model. In our previous work, we have initially constructed a macrothermodynamic model to reasonably explain why the reduction rate of hexavalent chromium [Cr(VI)] and the oxidation rate of 4-fluorophenol (4-FP) increase simultaneously in the complex photocatalytic system of Cr(VI) and 4-FP [50]. This is the basis for the comprehensive construction of advanced oxidation macrothermodynamic model in this paper. The significance of constructing the advanced oxidation macrothermodynamic model is to reasonably explain the known advanced oxidation reaction results and accurately predict the unknown advanced oxidation reaction results.

Firstly, in photocatalytic oxidation process, the reaction rate depends on the electron transfer efficiency from OPs (or lignin) to dissolved O_2. Electron transfer from OPs (or lignin) to dissolved O_2 can not be started without photocatalyst, so the photocatalytic oxidation reaction can not be carried out. In the presence of photocatalyst, the electron transfer from OPs (or lignin) to dissolved O_2 is turned on through the electron transfer function of photocatalyst, so the photocatalytic oxidation reaction can be carried out (Scheme 2a). Secondly, in the activated $KHSO_5$ oxidation process, photogenerated electrons or low-valence transition metal ions can activate $KHSO_5$ to generate singlet oxygen ($^1O_2$), which can directly react with OPs (or lignin) for redox reaction (Scheme 2b). There have been many reports on the study that $KHSO_5$ is activated by photogenerated electrons or low-valence transition metal ions to generate $^1O_2$

[51–54]. Thirdly, the synergistic advanced oxidation process can be understood as three steps. The first step is that photogenerated electrons and low-valence transition metal ions jointly activate $KHSO_5$ to produce $^1O_2$ through the electron-donating process. The second step is that the electron transfer function of photocatalyst accelerates the electron transfer from OPs (or lignin) to $^1O_2$. In the third step, the electron transfer function of photocatalyst starts the electron transfer from OPs (or lignin) to high-valence transition metal ions, and the high-valence transition metal ions are reduced back to low-valence states (Scheme 2c). Synergistic advanced oxidation process is an independent process with complete closed-loop reaction, and its oxidation efficiency is higher than that of photocatalytic oxidation and activated $KHSO_5$ oxidation. In the process of synergistic advanced oxidation, although $KHSO_5$ is activated by photogenerated electrons and low-valence transition metal ions at the same time, there is no clear quantitative relationship between the contribution of photogenerated electrons and low-valence transition metal ions to the activation of $KHSO_5$.

3.2.2. Unique advanced oxidation performance of Li(NiCoMn)-*x*/CNOCl powder photocatalysts and Li(NiCoMn)-10/CNOCl@PSA modular photocatalyst for the degradation of typical OPs in water through photocatalytic oxidation, activated $KHSO_5$ oxidation, and synergistic advanced oxidation processes

As shown in Fig. 4a, the electron transfer from RhB to dissolved O_2 can not be started without photocatalyst and in the presence of $Li(NiCoMn)O_2$, so RhB in water can not be degraded. RhB in water can be degraded in the presence of CNO and Li(NiCoMn)-*x*/CNOCl, and the degradation efficiency of RhB is gradually improved with increasing the $Li(NiCoMn)O_2$ dosage from 0 to 10 mg. However, the degradation efficiency of RhB gradually decreases when the dosage of $Li(NiCoMn)O_2$ continues to increase to 25 mg. This result shows that the electron transfer from RhB to dissolved O_2 is started in the presence of CNO and Li(NiCoMn)-*x*/CNOCl, and the electron transfer rate from RhB to dissolved O_2 is gradually accelerated with improving the photogenerated e^-–h^+ separation efficiency of photocatalyst. However, excessive addition of $Li(NiCoMn)O_2$ will lead to the agglomeration of Li(NiCoMn) metal ion clusters in the Li(NiCoMn)-*x*/CNOCl, which will reduce the ability of Li(NiCoMn) metal ion clusters to capture photogenerated electrons. In the quenching test of intermediate active species, we added silver nitrate ($AgNO_3$), benzoquinone (BQ), isopropanol (IPA), and triethanolamine (TEOA) to the photocatalytic oxidation system to quench photogenerated electrons (e^-), superoxide radicals ($*O_2^-$), hydroxyl radicals (*OH), and photogenerated holes (h^+). As shown in Fig. 4b, when BQ and TEOA are added to the photocatalytic oxidation system, the degradation efficiency of RhB decreases significantly, which indicates that $*O_2^-$ and h^+ play a key role in the photocatalytic oxidation process. When BQ is added to the photocatalytic oxidation system, it will undergo redox reaction with dissolved O_2, so BQ will indirectly consume $*O_2^-$ in the photocatalytic oxidation process. According to the advanced oxidation macrothermodynamic model shown in Scheme 2a, when the h^+ and dissolved O_2 in the photocatalytic oxidation system are consumed, the electron transfer from RhB to h^+ and from photogenerated electrons to dissolved O_2 is hindered, so the degradation efficiency of RhB is reduced. The above result shows that

the advanced oxidation macrothermodynamic model ignores the intermediate active species, but its results are consistent with those of the quenching test of intermediate active species. As shown in Fig. 4c, after adding a certain amount of $KHSO_5$ into the photocatalytic oxidation system, the degradation efficiency of RhB is significantly accelerated due to the synergistic advanced oxidation reaction is started. Based on the Scheme 2c in the advanced oxidation macrothermodynamic model, on the one hand, the electron transport from RhB to $^1O_2$ occurs at an ultra-fast speed due to the electron transport function of the photocatalyst, so that RhB in water is degraded at an ultra-fast speed. On the other hand, the electron transfer from RhB to high-valence transition metal ions through photocatalyst makes the high-valence transition metal ions reduced to low-valence states, so that the synergistic advanced oxidation reaction can continue. Because the synergistic advanced oxidation process has an ultra-fast reaction rate, in order to facilitate discussion, the concentration of $KHSO_5$ in the subsequent synergistic advanced oxidation test results is fixed at 2.5 mmol/L, and the addition amount is 1 mL. As shown in Fig. 4d, after adding $KHSO_5$ into the photocatalytic oxidation system, the photocatalytic activity of CNO is obviously improved, because $KHSO_5$ is activated by photogenerated electrons. In the dark state and in the presence of $KHSO_5$, CNO can slightly degrade RhB, while Li(NiCoMn)-10/CNOCl can degrade RhB transiently. This is because the low-valence transition metal ions in Li(NiCoMn)-10/CNOCl activate $KHSO_5$ to produce $^1O_2$, and the $^1O_2$ and RhB rapidly undergo redox reaction. However, the redox between $^1O_2$ and RhB quickly stops with the rapid oxidation of low-valence transition metal ions into high-valence states by $KHSO_5$. Under the condition of illumination and the existence of $KHSO_5$, Li(NiCoMn)-10/CNOCl shows extremely high activity due to the synergistic advanced oxidation effect. The pH value of actual organic wastewater is usually less than 7 or more than 7, and the influence of acidic or alkaline environment on the reaction efficiency of advanced oxidation is very significant. Therefore, we add 1 mL of 1 mol/L HCl or NaOH to the reaction system to study the influence of acidic or alkaline environment on photocatalytic oxidation or synergistic advanced oxidation process. As shown in Fig. 4e, the acidic environment has little effect on the degradation efficiency of RhB, while the alkaline environment significantly reduces the degradation efficiency of RhB, whether in photocatalytic oxidation or synergistic advanced oxidation process. On the one hand, there is a strong electrostatic binding between Li(NiCoMn) metal ion clusters and OH^-, which makes the Li(NiCoMn) metal ion clusters lose the ability to capture and conduct photogenerated electrons. On the other hand, $KHSO_5$ reacts with NaOH through the following equation, which makes the $KHSO_5$ lose the opportunity to be activated.

2KHSO+2NaOH=NaSO+KSO+2HO+O↑

As shown in Fig. 4f, in the synergistic advanced oxidation process, we add the quenching test of methanol (CH_3OH) on sulfate radical ($*SO_4^-$) and thought that BQ is a quencher for $^1O_2$. The result shows that h^+ and $^1O_2$ play a leading role in the synergistic advanced oxidation process, because without h^+ and $^1O_2$, the electron transfer from RhB to $^1O_2$ can not be carried out (Scheme 2c). Similar to the above photocatalytic oxidation mechanism, when BQ is added to the synergistic advanced oxidation

system, it will undergo redox reaction with dissolved O_2, so BQ will indirectly consume dissolved $^1O_2$ in the synergistic advanced oxidation process. According to the advanced oxidation macrothermodynamic model shown in Scheme 2c, when the h^+ and $^1O_2$ in the synergistic advanced oxidation system are consumed, the electron transfer from RhB to h^+ and from photogenerated electrons to $^1O_2$ is hindered, so the degradation efficiency of RhB is reduced. This result further verifies the consistency between the quenching test of intermediate active species and the advanced oxidation macrothermodynamic model. As shown in Figs. 4g and h, we replace RhB with CTC or LMG, and then repeat the experimental operation of Fig. 4d, and the experimental rules are exactly the same. This result shows that the as-prepared Li(NiCoMn)-*x*/CNOCl powder photocatalysts are universal for the degradation of OPs in water, and the constructed advanced oxidation macrothermodynamic model is generally suitable for the degradation of OPs in water through advanced oxidation technology. As shown in Figs. S3a–c, we have systematically optimized the synthesis conditions of the Li(NiCoMn)-10/CNOCl@PSA modular photocatalyst. The Li(NiCoMn)-10/CNOCl@PSA modular photocatalyst prepared under the optimum conditions shows similar activity to Li(NiCoMn)-10/CNOCl powder photocatalyst. There is no obvious change in the physical state of Li(NiCoMn)-10/CNOCl@PSA modular photocatalyst after use, which shows that the as-prepared Li(NiCoMn)-10/CNOCl@PSA modular photocatalyst has good mechanical stability (inset in Figs. S3a–c). As shown in Fig. 4i, the pure PSA carrier has no activity for the degradation of RhB. After the addition of $KHSO_5$, RhB was transiently degraded due to the activation of $KHSO_5$ by low-valence transition metal ions in PSA carrier. Compared with Fig. 4d, under the conditions of photocatalytic oxidation and synergistic advanced oxidation, the as-prepared Li(NiCoMn)-10/CNOCl@PSA modular photocatalyst shows similar activity to Li(NiCoMn)-10/CNOCl powder photocatalyst. As shown in Figs. S4a and b, after four photocatalytic oxidation cycles, Li(NiCoMn)-10/CNOCl and Li(NiCoMn)-10/CNOCl@PSA still maintain good activity, indicating that the as-prepared Li(NiCoMn)-10/CNOCl and Li(NiCoMn)-10/CNOCl@PSA have high stability. A small amount of activity loss can be attributed to a small amount of degradation intermediates adsorbed on the surface of photocatalyst, which makes the photocatalyst slightly poisoned. The leakage of Ni, Co, and Mn metal elements in different water environments from as-prepared Li(NiCoMn)-10/CNOCl and Li(NiCoMn)-10/CNOCl@PSA was detected by inductively coupled plasma-mass spectrometry (ICP-MS, Model: Thermo Scientific iCAP RQ). 1 mL of $KHSO_5$ (2.5 mmol/L), HCl (1 mol/L), or NaOH (1 mol/L) was added to 50 mL aqueous solution to construct different water environments, and then 10 mg of Li(NiCoMn)-10/CNOCl or one copy of Li(NiCoMn)-10/CNOCl@PSA was added respectively. After stirring the mixture for 12 hours, the photocatalyst was filtered out to obtain eight samples to be tested. As shown in Table S2, the Ni, Co, and Mn metal elements in the Li(NiCoMn)-10/CNOCl and Li(NiCoMn)-10/CNOCl@PSA hardly leak under the conditions of neutral, alkaline, or in the presence of $KHSO_5$, which shows that the as-prepared Li(NiCoMn)-10/CNOCl and Li(NiCoMn)-10/CNOCl@PSA have good stability under the conditions of neutral, alkaline, or in the presence of $KHSO_5$. However, under acidic conditions, some Ni, Co, and Mn metal elements in the Li(NiCoMn)-10/CNOCl and Li(NiCoMn)-10/CNOCl@PSA are leaked due to the leaching effect of metal elements in acidic environment.

3.2.3. Unique advanced oxidation performance of Li(NiCoMn)-*x*/CNOCl powder photocatalysts and Li(NiCoMn)-10/CNOCl@PSA modular photocatalyst for the production of vanillin by natural lignin depolymerization through photocatalytic oxidation, activated $KHSO_5$ oxidation, and synergistic advanced oxidation processes

In our previous work, we have systematically studied the product analysis and depolymerization mechanism of depolymerizing natural lignin from WCOSs through photocatalytic process [55]. Chemical components of final products from the photocatalytic conversion of WCOSs lignin were identified by gas chromatography–mass spectrometry (GC–MS), and there were 15 functionalized aromatics identified. Vanillin is the chemical with the most practical application value among 15 detected functionalized aromatics. In the study of depolymerization mechanism, we have made it clear that vanillin mainly comes from the efficient cleavage of Cα − C_β bonds in β − O − 4 substructures in WCOSs lignin during photocatalytic reaction.

We tested the activities of CNO, Li(NiCoMn)-10/CNOCl, Li(NiCoMn)-10/CNOCl@PSA, and PSA carrier to depolymerize natural lignin from WCOSs to produce vanillin under the conditions of photocatalytic oxidation, activated $KHSO_5$ oxidation, and synergistic advanced oxidation. As shown in Figs. S5a, b, and e, the activity of Li(NiCoMn)-10/CNOCl is greater than that of CNO and the activities of Li(NiCoMn)-10/CNOCl and Li(NiCoMn)-10/CNOCl@PSA are similar under the condition of photocatalytic oxidation. As shown in Figs. S5d and g, the activities of Li(NiCoMn)-10/CNOCl and Li(NiCoMn)-10/CNOCl@PSA are improved after adding $KHSO_5$ into the reaction system, because $KHSO_5$ is activated by photogenerated electrons and low-valence transition metal ions. As shown in Figs. S5c, f, and h, $KHSO_5$ can only be activated by low-valence transition metal ions in Li(NiCoMn)-10/CNOCl, Li(NiCoMn)-10/CNOCl@PSA, and PSA carrier under dark conditions, so Li(NiCoMn)-10/CNOCl, Li(NiCoMn)-10/CNOCl@PSA, and PSA carrier show the transient activities. The similar Y_R of vanillin in Figs. S5c, f, and h shows that the total amount of low-valence transition metal ions used to activate $KHSO_5$ in Li(NiCoMn)-10/CNOCl, Li(NiCoMn)-10/CNOCl@PSA, and PSA carrier is similar. The Li(NiCoMn) metal ion clusters in Li(NiCoMn)-10/CNOCl equivalently cover the Li(NiCoMn) metal ion clusters in PSA carrier in the Li(NiCoMn)-10/CNOCl@PSA modular photocatalyst.

4. Conclusions

In this paper, a series of Li(NiCoMn)-*x*/CNOCl powder photocatalysts and Li(NiCoMn)-10/CNOCl@PSA modular photocatalyst are successfully constructed by simple synthesis technology. For the Li(NiCoMn)-*x*/CNOCl powder photocatalysts, Li(NiCoMn) metal ion clusters or Cl^- directly or indirectly hinders the condensation of terminal $–NH_2$ and/or –OH groups, so the nanocage micromorphology is constructed. In addition, the introduced Li(NiCoMn) metal ion clusters can also improve the separation efficiency of photogenerated e^-–h^+ and activate $KHSO_5$. For the Li(NiCoMn)-10/CNOCl@PSA modular photocatalyst, it has photocatalytic activity similar to that of powder photocatalyst, and the Li(NiCoMn) metal ion clusters in the PSA carrier also have the effect of activating $KHSO_5$. The excellent performance of

Li(NiCoMn)-10/CNOCl@PSA modular photocatalyst and its convenient separation and reuse make it have potential engineering application value. The constructed advanced oxidation macrothermodynamic model is of great value in the theoretical research of advanced oxidation technology in the future.

Declarations

Conflict of Interest

The authors declare no conflict of interest.

Acknowledgments

This work was supported by the Central Government Guiding Local Science and Technology Development Fund Project, Hebei Province, the People's Republic of China (No. 254Z3603G) and the Natural Science Foundation of Hebei Province, China (No. B2020208090).

References

1. Janek, J., Zeier, W.G.: Challenges in speeding up solid-state battery development. Nat. Energy. **8**, 230–240 (2023)
2. Zhang, S., Li, S., Lu, Y.: Designing safer lithium-based batteries with nonflammable electrolytes: a review, eScience 1 163–177. (2021)
3. Ji, G., Wang, J., Liang, Z., Jia, K., Ma, J., Zhuang, Z., Zhou, G., Cheng, H.: Direct regeneration of degraded lithium-ion battery cathodes with a multifunctional organic lithium salt. Nat. Commun. **14**, 584 (2023)
4. Yang, T., Luo, D., Yu, A., Chen, Z.: Enabling future closed-loop recycling of spent lithium-ion batteries: direct cathode regeneration. Adv. Mater. **35**, 2203218 (2023)
5. Xu, P., Tan, D.H.S., Jiao, B., Gao, H., Yu, X., Chen, Z.: A materials perspective on direct recycling of lithium-ion batteries: principles, challenges and opportunities. Adv. Funct. Mater. **33**, 2213168 (2023)
6. Leal, V.M., Ribeiro, J.S., Coelho, E.L.D., Freitas, M.B.J.G.: Recycling of spent lithium-ion batteries as a sustainable solution to obtain raw materials for different applications. J. Energy Chem. **79**, 118–134 (2023)
7. Azimi, G., Chan, K.H.: A review of contemporary and emerging recycling methods for lithium-ion batteries with a focus on NMC cathodes. Resour. Conserv. Recy. **209**, 107825 (2024)
8. Qin, Z., Zhang, Y., Luo, W., Zhang, T., Wang, T., Ni, L., Wang, H., Zhang, N., Liu, X., Zhou, J., Chen, G.: A universal molten salt method for direct upcycling of spent Ni-rich cathode towards single-crystalline Li-rich cathode. Angew Chem. Int. Ed. **62**, e202218672 (2023)

9. Tong, Z., Li, Z., Tan, L., Li, Y., Wang, L., Shang, Y., Bi, J., Jiang, H., Lei, S., Zhu, W., Zhang, L.: Recent advances in synthesis and modification strategies for lithium-ion battery ternary cathodes. J. Energy Storage. **98**, 113085 (2024)
10. Tawonezvi, T., Zide, D., Nomnqa, M., Madondo, M., Petrik, L., Bladergroen, B.J.: Recovery of $Ni_xMn_yCo_z(OH)_2$ and Li_2CO_3 from spent Li-ionB cathode leachates using non-Na precipitant-based chemical precipitation for sustainable recycling. Chem. Eng. J. Adv. **17**, 100582 (2024)
11. Zhao, Z., Chen, J., Zhou, H., Hu, B., Meng, C., Yuan, A., Qiao, Y.: Engineering Mn-N_x sites on nitrogen-doped carbon spheres as efficient bifunctional electrocatalysts for zinc-air batteries. Met. Adv. **40**, 62–70 (2026)
12. Hao, Y., Chen, H., Zhou, H., Tang, M., Meng, C., Qiao, Y., Yuan, A., Guo, Q., Zhou, H.: A hydrophobic-zincophilic bifunctional interface enables stable Zn metal anode. Int. J. Min. Metall. Mater. (2026). https://doi.org/10.1007/s12613-026-3469-7
13. Wang, X., Maeda, K., Thomas, A., Takanabe, K., Xin, G., Carlsson, J.M., Domen, K., Antonietti, M.: A metal-free polymeric photocatalyst for hydrogen production from water under visible light. Nat. Mater. **8**, 76–80 (2009)
14. Huang, C., Chen, C., Zhang, M., Lin, L., Ye, X., Lin, S., Antonietti, M., Wang, X.: Carbon-doped BN nanosheets for metal-free photoredox catalysis. Nat. Commun. **6**, 7698 (2015)
15. Deng, A., Sun, Y., Gao, Z., Yang, S., Liu, Y., He, H., Zhang, J., Liu, S., Sun, H., Wang, S.: Internal electric field in carbon nitride-based heterojunctions for photocatalysis. Nano Energy. **108**, 108228 (2023)
16. Bai, L., Huang, H., Yu, S., Zhang, D., Huang, H., Zhang, Y.: Role of transition metal oxides in g-C_3N_4-based heterojunctions for photocatalysis and supercapacitors. J. Energy Chem. **64**, 214–235 (2022)
17. Liu, Y., Wang, X., Sun, Q., Chen, L., Yuan, M., Sun, Z., Zhang, Y., Xia, S., Zhao, J.: Enhanced activation of peroxymonosulfate by a floating Cu^0-MoS_2/C_3N_4 photocatalyst under visible-light assistance for tetracyclines degradation and *Escherichia coli* inactivation. Chem. Eng. J. **457**, 141220 (2023)
18. Zhao, J., Guo, H., Li, Y., Zheng, L., Ren, H., Zhao, L., Song, R.: Anchoring Ru nanoclusters to defect-rich polymeric carbon nitride as a bifunctional electrocatalyst for highly efficient overall water splitting. J. Mater. Chem. A. **11**, 18375–18386 (2023)
19. Ruan, Q., Bayazit, M.K., Kiran, V., Xie, J., Wang, Y., Tang, J.: Key factors affecting photoelectrochemical performance of g-C_3N_4 polymer films. Chem. Commun. **55**, 7191–7194 (2019)
20. Lau, V.W., Yu, V.W., Ehrat, F., Botari, T., Moudrakovski, I., Simon, T., Duppel, V., Medina, E., Stolarczyk, J.K., Feldmann, J., Blum, V., Lotsch, B.V.: Urea-modified carbon nitrides: enhancing photocatalytic hydrogen evolution by rational defect engineering. Adv. Energy Mater. **7**, 1602251 (2017)
21. Kumar, P., Singh, G., Guan, X., Lee, J., Bahadur, R., Ramadass, K., Kumar, P., Kibria, M.G., Vidyasagar, D., Yi, J., Vinu, A.: Multifunctional carbon nitride nanoarchitectures for catalysis. Chem. Soc. Rev. **52**, 7602–7664 (2023)

22. Betim, F.S., Coelho, E.L.D., Leal, V.M., Guimarães, B.Q., Magnago, L.B., Marins, A.A.L., Ferreira, S.A.D., Lelis, M.F.F., Freitas, M.B.J.G.: Green and sustainable recycling of $MnCo_2O_4/Mn_3O_4/Li(Mn_{0.75}Ni_{0.25})_2O_4$ mixed oxide from of spent Li-ion and Zn–MnO_2 batteries and evaluation of its photocatalytic properties. Sustain. Mater. Techno. **36**, e00624 (2023)
23. Wang, P., Sui, Y., Guan, J., Lou, X., Shen, J., Li, X., Guo, Y., Zhang, X., Song, X., Chen, Z., Wang, Z., Zhang, R.Q.: Efficient catalytic process induced by lithium-deficient spent $LiNi_{1/3}Co_{1/3}Mn_{1/3}O_2$: toward both organic pollutant decontamination and e-waste reuse. ACS EST. Water. **4**, 5150–5160 (2024)
24. Ma, Y., Gao, N., Quan, C., Norbert, M.: H_2-rich syngas production through separator pyrolysis over $LiNi_{1/3}Co_{1/3}Mn_{1/3}O_2$ pre-catalysts derived from spent lithium-ion batteries. Waste Manage. **211**, 115268 (2026)
25. Deng, J., Li, H., Wang, S., Ding, D., Chen, M., Liu, C., Tian, Z., Novoselov, K.S., Ma, C., Deng, D., Bao, X.: Multiscale structural and electronic control of molybdenum disulfide foam for highly efficient hydrogen production. Nat. Commun. **8**, 14430 (2017)
26. Li, X., Pan, X., Yu, L., Ren, P., Wu, X., Sun, L., Jiao, F., Bao, X.: Silicon carbide-derived carbon nanocomposite as a substitute for mercury in the catalytic hydrochlorination of acetylene. Nat. Commun. **5**, 3688 (2014)
27. Liu, Y., Yang, F., Zhang, Y., Xiao, J., Yu, L., Liu, Q., Ning, Y., Zhou, Z., Chen, H., Huang, W., Liu, P., Bao, X.: Enhanced oxidation resistance of active nanostructures via dynamic size effect. Nat. Commun. **8**, 14459 (2017)
28. Pati, P.B., Damas, G., Tian, L., Fernandes, D.L.A., Zhang, L., Pehlivan, I.B., Edvinsson, T., Araujo, C.M., Tian, H.: An experimental and theoretical study of an efficient polymer nano-photocatalyst for hydrogen evolution. Energy Environ. Sci. **10**, 1372–1376 (2017)
29. Pavliuk, M.V., Wrede, S., Liu, A., Brnovic, A., Wang, S., Axelsson, M., Tian, H.: Preparation, characterization, evaluation and mechanistic study of organic polymer nano-photocatalysts for solar fuel production. Chem. Soc. Rev. **51**, 6909–6935 (2022)
30. Li, Z., Li, B., Li, Q.: Single-atom nano-islands (SANIs): a robust atomic–nano system for versatile heterogeneous catalysis applications. Adv. Mater. **35**, 2211103 (2023)
31. Li, K., Yan, L., Zeng, Z., Luo, S., Luo, X., Liu, X., Guo, H., Guo, Y.: Fabrication of $H_3PW_{12}O_{40}$-doped carbon nitride nanotubes by one-step hydrothermal treatment strategy and their efficient visible-light photocatalytic activity toward representative aqueous persistent organic pollutants degradation. Appl. Catal. B: Environ. 156–157 141–152. (2014)
32. Li, K., Zeng, Z., Yan, L., Luo, S., Luo, X., Huo, M., Guo, Y.: Fabrication of platinum-deposited carbon nitride nanotubes by a one-step solvothermal treatment strategy and their efficient visible-light photocatalytic activity. Appl. Catal. B: Environ. **165**, 428–437 (2015)
33. Li, K., Zeng, Z., Yan, L., Huo, M., Guo, Y., Luo b, S., Luo, X.: Fabrication of C/X-TiO_2@C_3N_4 NTs (X = N, F, Cl) composites by using phenolic organic pollutants as raw materials and their visible-light

photocatalytic performance in different photocatalytic systems. Appl. Catal. B: Environ. **187**, 269–280 (2016)

34. Shi, L., Huang, G., Wang, Z., Duan, Y., Zhang, Y., Chen, J., Li, W., Yu, H., Elimelech, M.: Dual-substrate synergistic catalysis for highly efficient water purification. Nat. Water. **3**, 345–353 (2025)
35. Guo, Q., Yu, X., Zhang, K., Xia, L., Liu, S., Zhang, W., Du, Y., Tang, H., Peng, Y., Li, Z., Duan, L., Yang, X.: Atomically dispersed Co-Mn dual sites anchored in photoresponsive carbon nitride mediated peroxymonosulfate activation for elimination of petroleum hydrocarbon in water. Appl. Catal. B: Environ. **343**, 123581 (2024)
36. Jing, M., Zhao, H., Jian, L., Pan, C., Dong, Y., Zhu, Y.: Coral-like B-doped g-C_3N_4 with enhanced molecular dipole to boost photocatalysis-self-Fenton removal of persistent organic pollutants. J. Hazard. Mater. **449**, 131017 (2023)
37. Shi, H., He, Y., Li, Y., Luo, P.: Unraveling the synergy mechanism between photocatalysis and peroxymonosulfate activation on a Co/Fe bimetal-doped carbon nitride. ACS Catal. **13**, 8973–8986 (2023)
38. Rastogi, A., Al-Abed, S.R., Dionysiou, D.D.: Sulfate radical-based ferrous–peroxymonosulfate oxidative system for PCBs degradation in aqueous and sediment systems. Appl. Catal. B: Environ. **85**, 171–179 (2009)
39. Soltani, T., Tayyebi, A., Lee, B.K.: Quick and enhanced degradation of bisphenol A by activation of potassium peroxymonosulfate to $SO_4{\cdot}^-$ with Mn-doped $BiFeO_3$ nanoparticles as a heterogeneous Fenton-like catalyst. Appl. Surf. Sci. **441**, 853–861 (2018)
40. Pornrungroj, C., Annuar, A.B.M., Wang, Q., Rahaman, M., Bhattacharjee, S., Andrei, V., Reisner, E.: Hybrid photothermal–photocatalyst sheets for solar-driven overall water splitting coupled to water purification. Nat. Water. **1**, 952–960 (2023)
41. Wang, Q., Warnan, J., Rodríguez-Jiménez, S., Leung, J.J., Kalathil, S., Andrei, V., Domen, K., Reisner, E.: Molecularly engineered photocatalyst sheet for scalable solar formate production from carbon dioxide and water. Nat. Energy. **5**, 703–710 (2020)
42. Wang, J., Zhang, J., Li, Y., Xia, X., Yang, H., Kim, J.H., Zhang, W.: Silver single atoms and nanoparticles on floatable monolithic photocatalysts for synergistic solar water disinfection. Nat. Commun. **16**, 981 (2025)
43. Lu, P., Liu, K., Liu, Y., Ji, Z., Wang, X., Hui, B., Zhu, Y., Yang, D., Jiang, L.: Heterostructure with tightly-bound interface between In_2O_3 hollow fiber and $ZnIn_2S_4$ nanosheet toward efficient visible light driven hydrogen evolution. Appl. Catal. B: Environ. Energy. **345**, 123697 (2024)
44. Rahimi, A., Ulbrich, A., Coon, J.J., Stahl, S.S.: Formic-acid-induced depolymerization of oxidized lignin to aromatics. Nature. **515**, 249–252 (2014)
45. Chen, C., Ji, X., Xiong, Y., Jiang, J.: Environmentally-friendly preparation of natural hollow carbon spheres derived from a biomass puffball for *in situ* upgrading of lignin-derived vanillin. Green. Chem. **26**, 1488–1500 (2024)

46. Zirbes, M., Graßl, T., Neuber, R., Waldvogel, S.R.: Peroxodicarbonate as a green oxidizer for the selective degradation of kraft lignin into vanillin. Angew Chem. Int. Ed. **62**, e202219217 (2023)
47. Zeng, Z., Li, K., Wei, K., Dai, Y., Yan, L., Guo, H., Luo, X.: Fabrication of porous g-C_3N_4 and supported porous g-C_3N_4 by a simple precursor pretreatment strategy and their efficient visible-light photocatalytic activity. Chin. J. Catal. **38**, 498–508 (2017)
48. Zeng, Z., Li, K., Wei, K., Dai, Y., Yan, L., Guo, H., Luo, X.: Fabrication of highly dispersed platinum-deposited porous g-C_3N_4 by a simple in situ photoreduction strategy and their excellent visible light photocatalytic activity toward aqueous 4-fluorophenol degradation. Chin. J. Catal. **38**, 29–38 (2017)
49. Zeng, D., Li, Y.: Precisely loading Pt on Tb_4O_7/CN heterojunction for efficient photocatalytic overall water splitting: design and mechanism. Appl. Catal. B: Environ. **342**, 123393 (2024)
50. Li, K., Zhao, D., Li, Y., Luo, S., Zhou, Z.: The synergistic photocatalytic effects of surface-modified g-C_3N_4 in simple and complex pollution systems based on a macro-thermodynamic model. Environ. Sci. : Nano. **8**, 217–232 (2021)
51. Wu, Y., Hao, C., Lu, Z., Liu, X., Jiang, W., Zhou, L., Wang, X., Zhou, L., Lei, J., Zhang, J., Liu, Y.: Tailoring COFs for highly selective generation of singlet oxygen to boost antibiotic removal: Spatial regulation of PMS and photogenerated carriers. Water Res. **297**, 125653 (2026)
52. Fan, C., Yuan, C., Gao, L., Jia, P., Zhang, Y., Huang, H., Tian, N.: Switching peroxomonosulfate activation to a non-radical dominant pathway by a photo-driven Bi^0 mediator in an S-scheme heterojunction. J. Mater. Chem. A. **14**, 9573–9585 (2026)
53. Cheng, Q., Tu, Y., Nengzi, L., Guo, X., Gong, Z., Du, E., Peng, M., Advanced, C.: N and P removal performance and mechanism of municipal wastewater in lab-scale denitrifying filter for generating biogenic manganese oxides. Sep. Purif. Technol. **362**, 131855 (2025)
54. Zhu, G., Li, W., Dou, A., Xu, Q., Zhu, M.: Singlet oxygen mediated ciprofloxacin degradation via manganese-doped cobalt oxide catalysis with peroxymonosulfate for water purification. J. Colloid Interf Sci. **702**, 138861 (2026)
55. Ku, C., Li, K., Guo, H., Wu, Q., Yan, L.: One-step construction of mesoporous cyano and sulfur co-modified carbon nitride for photocatalytic valorization of lignin to functionalized aromatics, Appl. Surf. Sci. 592 153266.

Figures

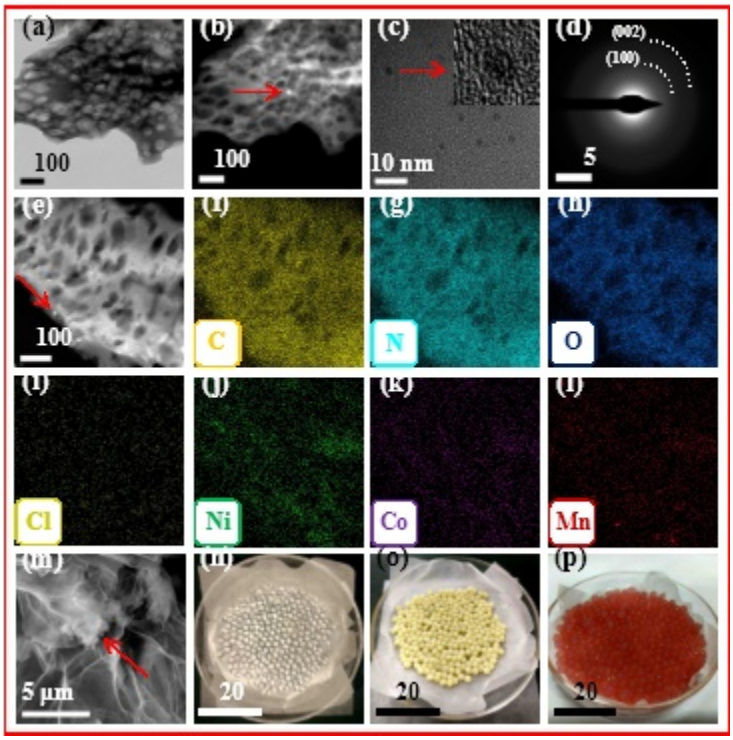


Figure 1

TEM (a), TEM-HAADF (b and e), HRTEM (c), SAED (d), and EDX elemental mapping (f–l) images of Li(NiCoMn)-10/CNOCl; FESEM image of Li(NiCoMn)-10/CNOCl@PSA observed from cross-section (m);

physical photos of pure PSA carrier (n), Li(NiCoMn)-10/CNOCl@PSA (o), and adsorption-saturated Li(NiCoMn)-10/CNOCl@PSA (p).

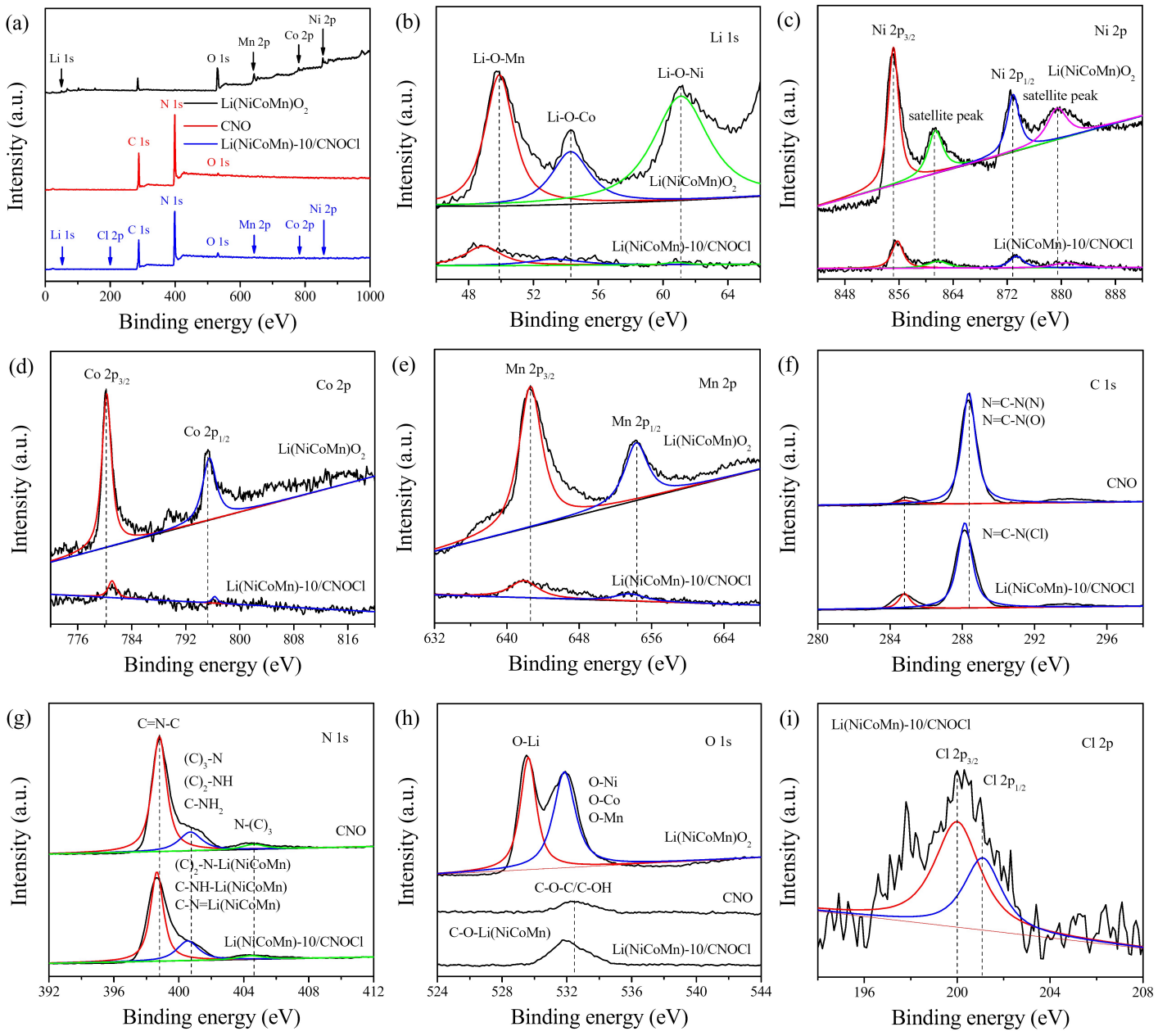


Figure 2

Full XPS (a) and high-resolution XPS (b-i) of Li(NiCoMn)O_2, CNO, and Li(NiCoMn)-10/CNOCl in the Li 1s, Ni 2p, Co 2p, Mn 2p, C 1s, N 1s, O 1s, and Cl 2p binding energy regions.

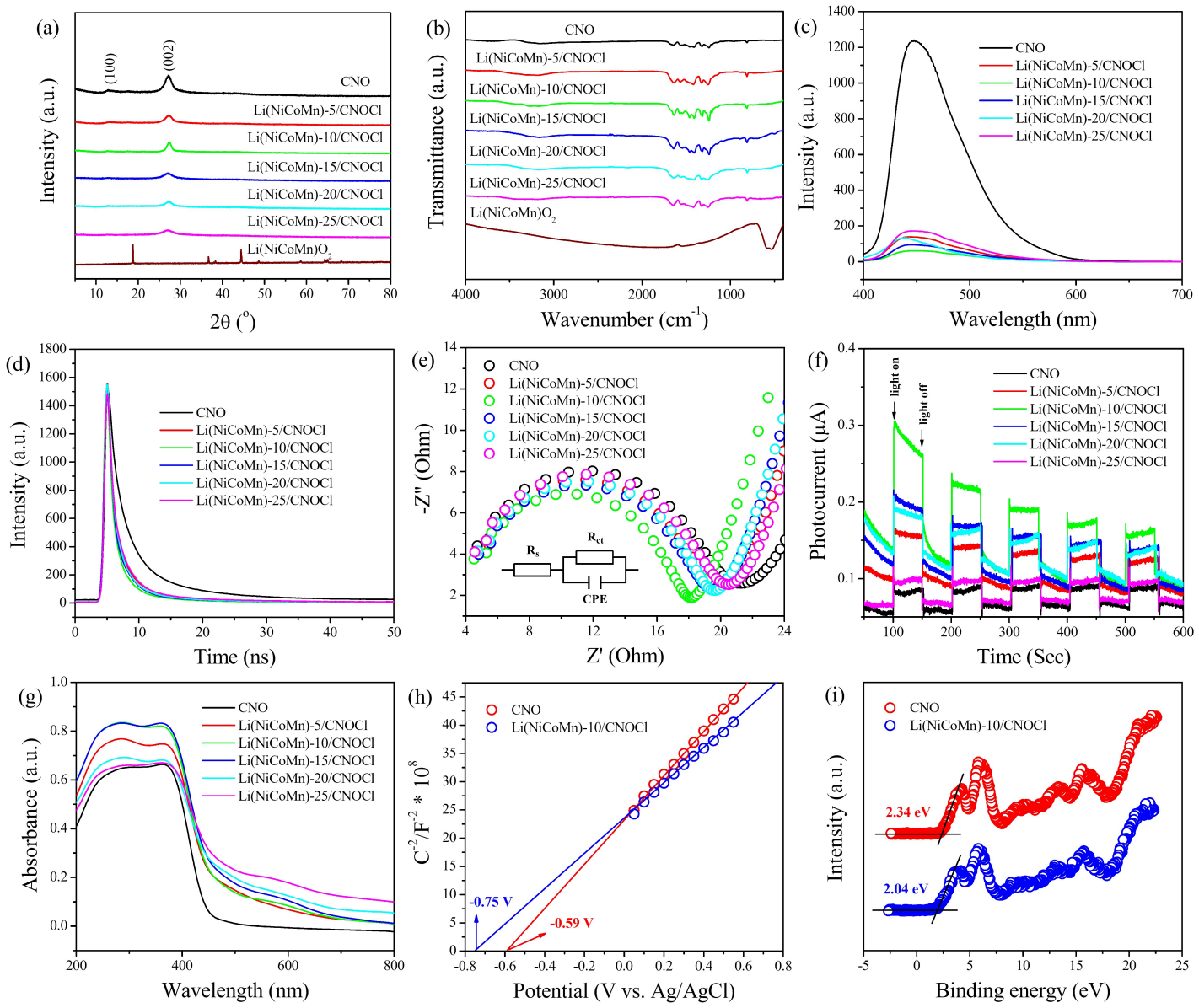


Figure 3

XRD patterns (a), FT-IR spectra (b), PL spectra (c), TR-PL spectra (d), EIS (e), transient photocurrent (f), UV–vis/DRS (g), Mott-Schottky plots (h), and VB-XPS (i) of as-prepared CNO and Li(NiCoMn)-*x*/CNOCl.

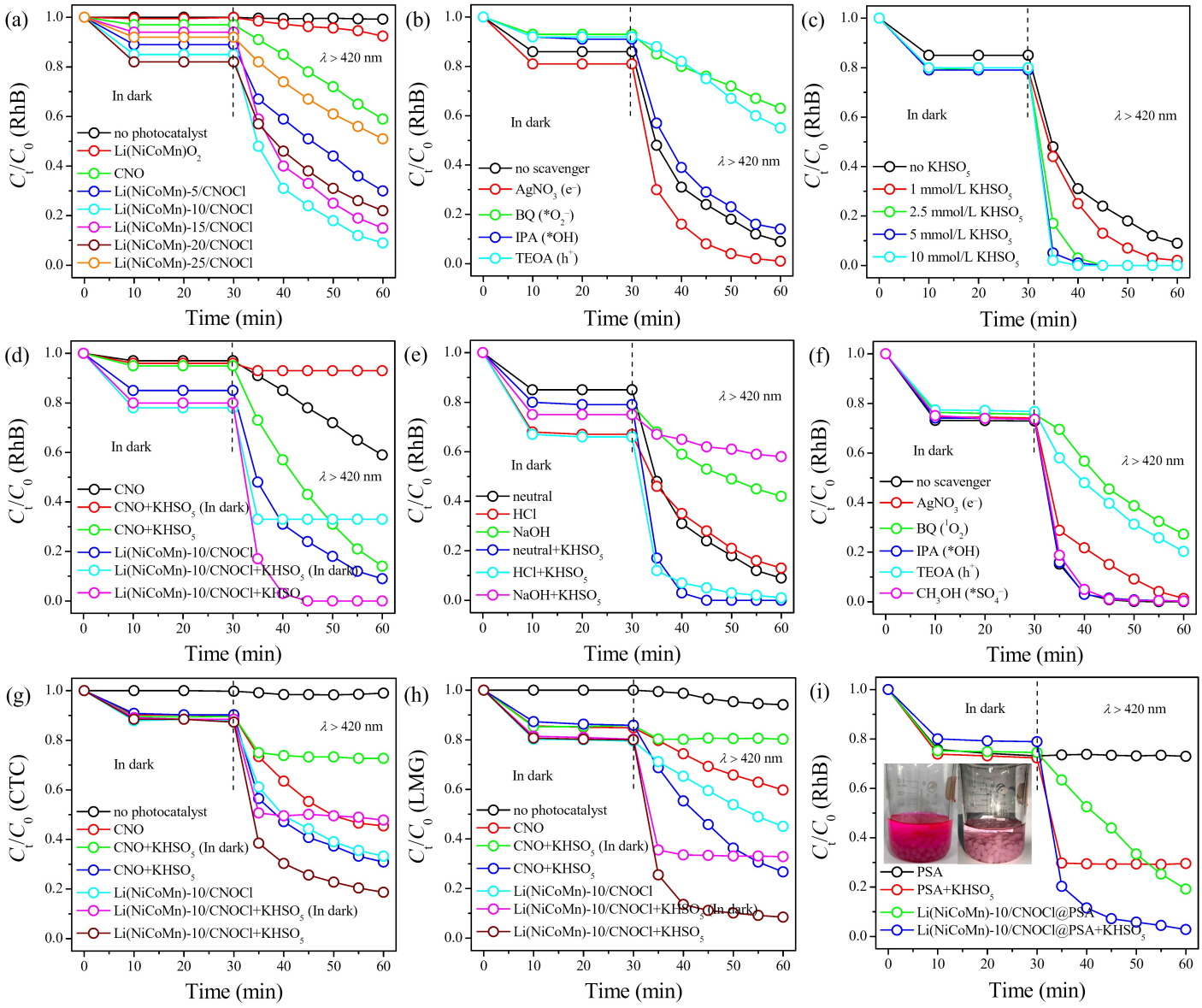


Figure 4

Degradation of RhB in water through photocatalytic oxidation, activated $KHSO_5$ oxidation, and synergistic advanced oxidation processes by using as-prepared CNO and Li(NiCoMn)-*x*/CNOCl powder photocatalysts: effect of Li(NiCoMn)O_2 dosage on the activities of Li(NiCoMn)-*x*/CNOCl in the photocatalytic oxidation process (a), effects of various scavengers on the activity of Li(NiCoMn)-10/CNOCl in the photocatalytic oxidation process (b), effect of $KHSO_5$ concentration on the activity of Li(NiCoMn)-10/CNOCl in the synergistic advanced oxidation process (c), effect of $KHSO_5$ on the activities of CNO and Li(NiCoMn)-10/CNOCl under dark and light conditions (d), effect of acid or alkali environment on the activity of Li(NiCoMn)-10/CNOCl in the photocatalytic oxidation and synergistic advanced oxidation processes (e), effects of various scavengers on the activity of Li(NiCoMn)-10/CNOCl in the synergistic advanced oxidation process (f); degradation of CTC (g) and LMG (h) in water through photocatalytic oxidation, activated $KHSO_5$ oxidation, and synergistic advanced

oxidation processes by using as-prepared CNO and Li(NiCoMn)-10/CNOCl powder photocatalysts; effect of $KHSO_5$ on the activities of PSA carrier and Li(NiCoMn)-10/CNOCl@PSA modular photocatalyst (inlet image on the left: Li(NiCoMn)-10/CNOCl@PSA in the aqueous RhB before illumination, inlet image on the right: Li(NiCoMn)-10/CNOCl@PSA in the aqueous RhB after illumination) (i).

Supplementary Files

This is a list of supplementary files associated with this preprint. Click to download.

- GraphicalAbstract.doc
- SupplementaryMaterial.doc
- Scheme.docx